Analysis and Comparison of the Radiated Electromagnetic Interference Generated by Power Converters With Si MOSFETs and GaN HEMTs

Yingjie Zhang, *Student Member, IEEE*, Shuo Wang, *Fellow, IEEE*, and Yongbin Chu

***Abstract*—In this article, the effects of the parameters of GaN HEMTs and Si MOSFETs and the load conditions on the radiated electromagnetic interference (EMI) are analyzed based on the compositions of the equivalent noise voltage sources. These compositions include the rising and falling edges of the switching voltages, the zero-voltage-switching voltage drops and the parasitic ringing. The radiated EMI from two identical dual-active bridge converters with GaN HEMTs and Si MOSFETs is investigated and compared. Experiments were conducted to validate the analysis.**

***Index Terms*—GaN HEMT, power converter, radiated electromagnetic interference (EMI), Si MOSFET.**

I. Introduction

GaN HEMTs become popular in the field of power electronics due to their superior performance in many aspects, such as the higher breakdown voltage [1]–[3], higher efficiency [4], [5], better thermal conductivity [6], and so on, than Si MOSFETs. However, their abilities of achieving higher switching frequencies and faster switching speeds than Si MOSFETs lead to severer electromagnetic interference (EMI) issues, especially the radiated EMI in the high-frequency range [7], [8], than Si MOSFETs.

Some research has been conducted to investigate the difference of switching characteristics and the generated electromagnetic interference (EMI) between the GaN HEMT and the Si MOSFET. Huang *et al.* [4] analyzed the influence of reverse recovery charge and the output capacitance on the turn-ON transient, whereas it focused on the difference of switching power loss between GaN HEMTs and Si MOSFETs. The authors in [6] and [9] compared the conducted EMI generated by converters with GaN HEMTs and Si MOSFETs. However, it did not further thoroughly analyze the mechanisms for the difference. There are few papers addressing radiated EMI for GaN HEMTs and Si MOSFETs.

Manuscript received September 2, 2019; revised December 16, 2019; accepted January 25, 2020. Date of publication February 7, 2020; date of current version April 22, 2020. This work was supported by the Texas Instruments Inc. Recommended for publication by Associate Editor F. Luo. *(Corresponding author: Shuo Wang.)*

Yingjie Zhang and Shuo Wang are with the University of Florida, Gainesville, FL 32611 USA (e-mail: zhangyingjie@ufl.edu; shuowang@ieee.org).

Yongbin Chu is with the Texas Instruments Inc., Dallas, TX 75243 USA (e-mail: y-chu4@ti.com).

Color versions of one or more of the figures in this article are available online at http://ieeexplore.ieee.org.

Digital Object Identifier 10.1109/TPEL.2020.2972342

Besides, the load condition influences the switching speed of the switches so it is another key factor affecting the radiated EMI. Under heavy load, the switching speed mainly depends on the driving loop, while the power loop dominates under light load. The switching characteristics of the Si MOSFETs have been discussed in many papers [10]–[13], while the influence of the load condition is not covered in most of them. The authors in [14] and [15] claimed there are three possible cases of the switching transients, but the mechanism and the parasitics involved were not analyzed. When it comes to the wide bandgap (WBG) devices, [16] and [17] derived the equations of the rising/falling speed for the GaN HEMTs and they are different from the conventional equations used for the Si MOSFETs. However, the clear explanation of the equation difference between GaN HEMTs and Si MOSFETs was not given in the papers. Moreover, [18] developed two models for the WBG devices based on the two possible cases in the switching transients, but it concentrated on the analysis of the power loss.

This article analyzes the effect of the parasitic parameters of the semiconductor switches on the switching characteristics, and the effects of the switching characteristics and the load condition on the radiated EMI. Based on the analysis, the radiated EMI generated by the dual-active bridge (DAB) converters with GaN HEMTs and Si MOSFETs under different load conditions are compared. This article is organized as follows. In Section II, the radiation model of the DAB converter is first developed. Based on the developed model, the difference of switching waveforms between the converters with Si MOSFETs and GaN HEMTs leads to the difference of radiated EMI. Therefore, the relationship of the radiated EMI and the compositions of the switching waveforms are investigated. In Section III, the effects of switching parameters of the Si MOSFET and the GaN HEMT on the compositions of switching waveforms are analyzed. The radiated EMI is finally measured and compared in Section IV to verify the analysis. Meanwhile, the variation of the radiated EMI while changing the parasitic parameters is analyzed to further verify the analysis. Finally, Section V concludes this article.

II. Radiation Model of a DAB Converter and the Compositions of Noise Voltage Sources

Two DAB converters were built with Si MOSFETs and GaN HEMTs, respectively to compare the radiated EMI generated by the converters with the two devices, as shown in Fig. 1. The

0885-8993 © 2020 IEEE. Personal use is permitted, but republication/redistribution requires IEEE permission.
See https://www.ieee.org/publications/rights/index.html for more information.

Authorized licensed use limited to: University of Florida. Downloaded on December 30,2020 at 03:23:17 UTC from IEEE Xplore. Restrictions apply.

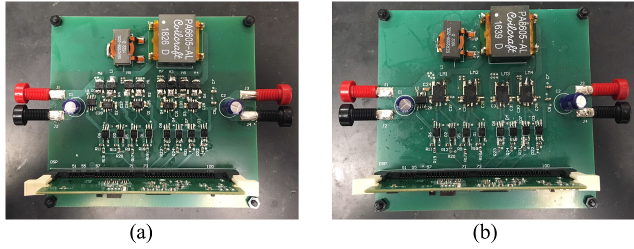

Fig. 1. Prototypes of DAB converters with (a) Si MOSFETs (b) GaN HEMTs.

TABLE I
PARAMETERS OF THE SI MOSFET AND GaN HEMT

		Si MOSFET IRF7493	GaN HEMT LMG5200
V_{DS_max} (V)		80	80
I_{D_max} (A)		9.3	10
R_{on} (mΩ)		15	15
V_{th} (V)		2	2
R_g (Ω)		2.5	2.5
C_{iss} (pF) (V_{DS}=15V)		1600	420
C_{oss} (pF)	V_{DS}=15V	410	400
	V_{DS}=30V	290	270
C_{GD} (pF) (V_{DS}=15V)		150	10
K(A/V^2)		15	61
Package		SO-8	QFM

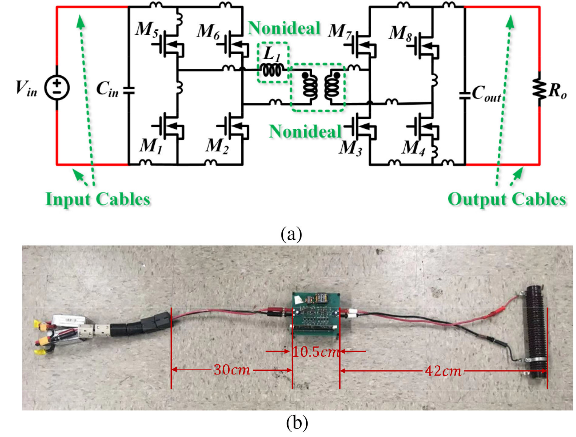

Fig. 2. Schematic and prototype of the DAB converter. (a) Schematics including parasitic inductances on switching branches. (b) Prototype including cables and load.

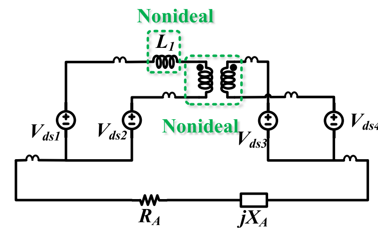

Fig. 3. Radiation model of the DAB converter.

two converters are identical except the semiconductor switches. Because they use identical components and have an identical printed circuit board layout, all the parasitic parameters are equal. Also, the drivers of both converters supply enough driving current, so the switching speed of devices is not limited by the driving.

The switching frequency of the converters is 735 kHz. The input and output voltages are both 30 V. The maximum output power is 150 W. The model numbers and parameters of the Si MOSFETs and GaN HEMTs are in Table I. Due to the limited options of low-voltage-enhanced GaN HEMT, the two GaN HEMTs of a half bridge are integrated with the drivers, while the MOSFETs and their IC drivers are separated.

Fig. 2(a) is the schematics of the DAB converter including parasitic inductance in each switching branches. Fig. 2(b) is the prototype with input, output cables, battery, and a load resistor. There are high impedance ferrite beads on the battery end to isolate the battery from the input cable [19], so the cable antenna's impedance is not influenced by the complicated structure of the battery. Based on the topology of the DAB converter in Fig. 2(a), its radiation model can be developed in Fig. 3 [19].

Based on the theory developed in [19], in Fig. 3, $V_{\rm ds1} \sim V_{\rm ds4}$ are the drain-to-source voltages of $M_1 \sim M_4$, respectively. And they are the noise sources to generate the radiated EMI. Meanwhile, R_A and jX_A are the resistance and reactance of the antenna, respectively, consisting of converter's input and output cables.

According to the radiation model and the antenna theory [20], the radiated electric field generated by the DAB converter is derived in (1) based on the superposition theory

$$E_{\max} = \sqrt{\frac{\eta G_o R_A}{4\pi r^2}} \times \frac{V_{\rm ds1}VG_1 + V_{\rm ds2}VG_2 + V_{\rm ds3}VG_3 + V_{\rm ds4}VG_4}{\sqrt{R_A^2 + X_A^2}} \quad (1)$$

where η is the intrinsic impedance of the free space, and G_o is the maximum gain of the antenna. $VG_1 \sim VG_4$ are the voltage gains from noise sources $V_{\rm ds1} \sim V_{\rm ds4}$ to the induced voltages on the antenna due to each source, respectively. The radiated electric field is measured at distance r, which could be 3 or 10 m defined in standards [7], [8].

Based on Fig. 3 and (1), since the passive components and the layout of the two converters are identical, the difference of radiated EMI between the two converters is exclusively caused by the difference of voltage sources $V_{\rm ds1} \sim V_{\rm ds4}$, which is related to the characteristics of Si MOSFETs and GaN HEMTs.

To analyze the difference of source voltages generated by converters with Si MOSFETs and GaN HEMTs, $V_{\rm ds1} \sim V_{\rm ds4}$ of the two converters are measured with an oscilloscope – Rigol MSO 4054 (500-MHz bandwidth). Meanwhile, to investigate the effects of load conditions on the radiated EMI, the converters were tested under two different load conditions, i.e., when the

Authorized licensed use limited to: University of Florida. Downloaded on December 30,2020 at 03:23:17 UTC from IEEE Xplore. Restrictions apply.

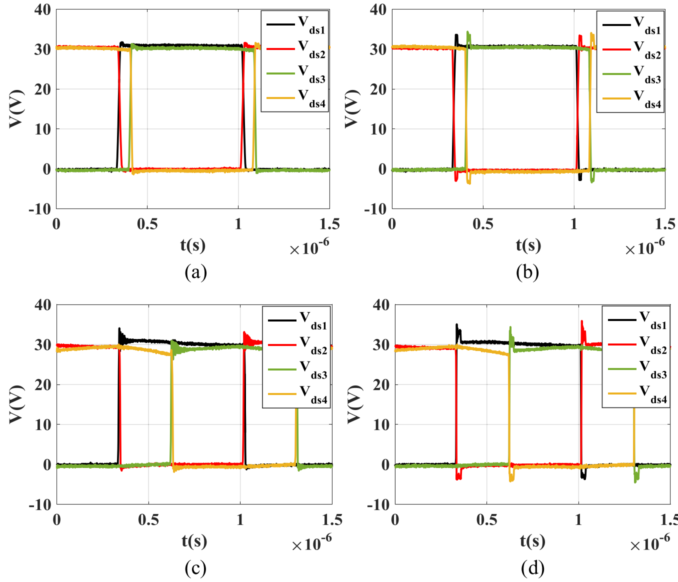

Fig. 4. Waveforms of voltage sources $V_{\rm ds1} \sim V_{\rm ds4}$. (a) Si MOSFETs when the output power is 49 W. (b) GaN HEMTs when the output power is 49 W. (c) Si MOSFETs when the output power is 132 W. (d) GaN HEMTs when output power is 132 W.

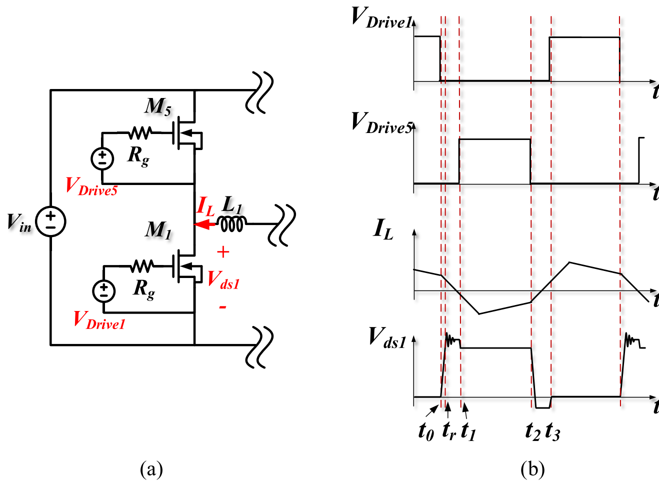

Fig. 5. Half bridge consisting of M_1 and M_5. (a) Schematic and (b) operating waveforms.

output power is 49 and 132 W. The measured waveforms are in Fig. 4.

Because $V_{\rm ds1} \sim V_{\rm ds4}$ are generated similarly by four switching legs in Fig. 2 [21], $V_{\rm ds1}$, which is generated by the half bridge consisting of M_1 and M_5 in Fig. 5(a), is taken as an example. The driving voltage waveforms $V_{\rm Drive1}$ and $V_{\rm Drive5}$ of the switches M_1 and M_5, the drain-to-source voltage waveform $V_{\rm ds1}$ of M_1 and inductor current I_L are shown in Fig. 5(b) for illustrating purpose.

Based on the superposition theory, the time-domain waveform of $V_{\rm ds1}$ can be separated into the following three compositions illustrated in Fig. 6.

1) *Trapezoidal waveform* $V_{ds1_{\rm Trapezoidal}}$*:* The trapezoidal waveform is the basic composition of the noise voltage sources to realize the function of the converter. It is generated by the turning ON and OFF of the switches.

2) *Zero-voltage-switching (ZVS) waveform* $V_{\rm ds1_ZVS}$*:* During the dead times $t_0 \sim t_1$ and $t_2 \sim t_3$ in Fig. 5(b), both the driving signals are zero. However, one of the switches reversely conducts current before it is turned ON. Therefore, ZVS can be achieved. The ZVS waveform is, therefore, caused by the reverse conduction of the switches.

3) *Ringing waveform* $V_{\rm ds1_Ringing}$*:* The ringing is induced by the resonance of parasitic parameters and their initial conditions.

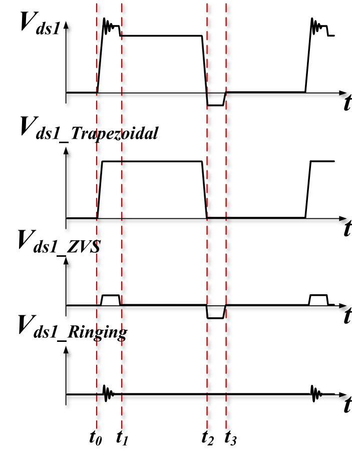

Fig. 6. Composition of $V_{\rm ds1}$.

Therefore, the waveform of $V_{\rm ds1}$ is the sum of the three compositions

$$V_{\rm ds1} = V_{\rm ds1_Trapezoidal} + V_{\rm ds1_ZVS} + V_{\rm ds1_Ringing}. \quad (2)$$

Based on the linearity of the Fourier transform $\mathcal{F}()$, the spectrum $\mathcal{F}(V_{\rm ds1})$ of V_{ds1} is the sum of the spectra $\mathcal{F}(V_{\rm ds1_Trapezoidal})$, $\mathcal{F}(V_{\rm ds1_ZVS})$, and $\mathcal{F}(V_{\rm ds1_Ringing})$ of the three compositions as

$$\mathcal{F}(V_{\rm ds1}) = \mathcal{F}(V_{\rm ds1_Trapezoidal}) + \mathcal{F}(V_{\rm ds1_ZVS}) + \mathcal{F}(V_{\rm ds1_Ringing}). \quad (3)$$

The aforementioned analysis is also valid for the other three voltage sources $V_{\rm ds2} \sim V_{\rm ds4}$.

The three compositions of $V_{\rm ds1}$ are extracted to illustrate their influence on the spectrum of the total noise source voltage. The time-domain waveforms and the spectra of $V_{\rm ds1}$ and its compositions with different devices under different load conditions are shown in Fig. 7 in different colors. Due to the bandwidth limitation of the oscilloscope, the measured spectrum is up to 500 MHz.

From Fig. 7, the trapezoidal waveform is generally dominant in the low-frequency range, and the ringing always takes over at high frequencies.

In addition, under the same load condition, the source voltage spectrum on the GaN HEMT is larger than that on the Si MOSFET. While for the same device, the source voltage spectrum with heavy load is higher than that with light load.

Authorized licensed use limited to: University of Florida. Downloaded on December 30,2020 at 03:23:17 UTC from IEEE Xplore. Restrictions apply.

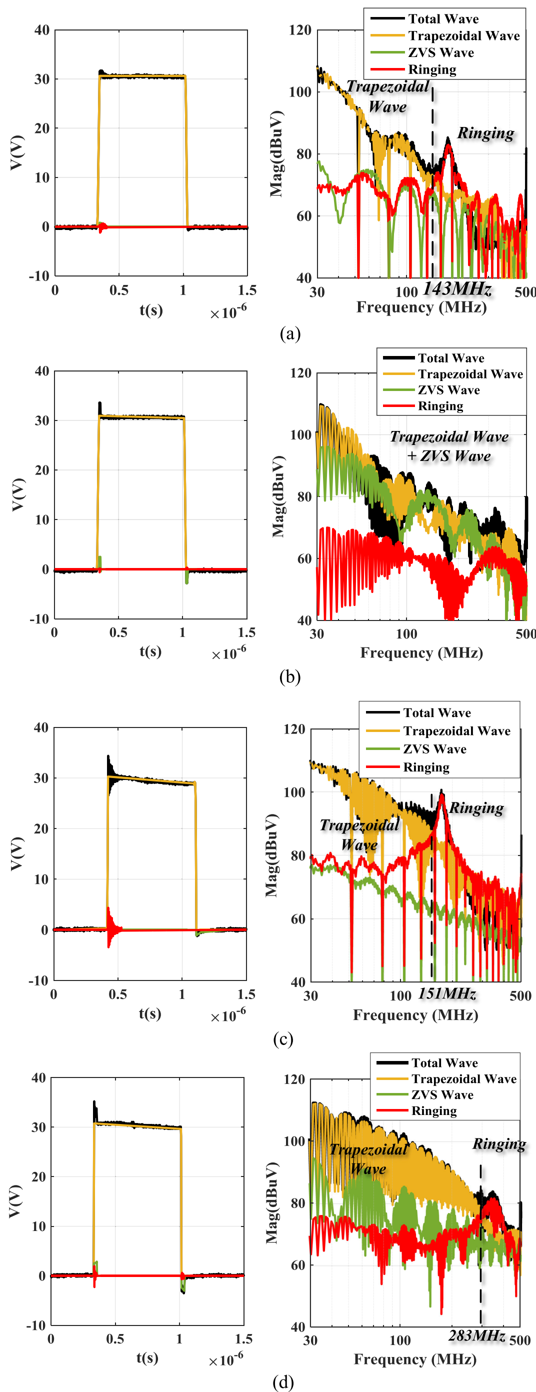

Fig. 7. Waveform and spectra of $V_{\rm ds1}$ and its three compositions. (a) Si MOSFETs when the output power is 49 W. (b) GaN HEMTs when the output power is 49 W. (c) Si MOSFETs when the output power is 132 W. (d) GaN HEMTs when the output power is 132 W.

III. Effects of Parameters of Si MOSFETs and GaN HEMTs on Source Voltage Spectrum and Radiated EMI

As analyzed in Section II, the source voltage spectrum is determined by three compositions. At the same time, the three compositions are affected by the parameters of Si MOSFETs and the GaN HEMTs, so the three compositions of $V_{\rm ds1}$ will be investigated with device parameters.

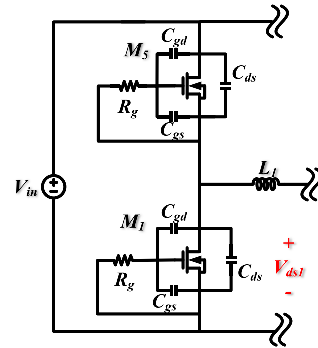

Fig. 8. Schematic of half bridge consisting of M_1 and M_5 with parasitic capacitance.

A. Trapezoidal Waveform

1) Theoretical Analysis: The magnitudes of trapezoidal waveforms of $V_{\rm ds1} \sim V_{\rm ds2}$ and $V_{\rm ds3} \sim V_{\rm ds4}$ are equal to the input and output voltages, respectively. They are 30 V, and their frequencies are equal to the switching frequency 735 kHz. And the duty cycles are all close to 50%. Therefore, the only parameter differentiating the trapezoidal waveforms between Si MOSFETs and GaN HEMTs under various load conditions is the rising/falling time, which is determined by the switching speed.

Some papers analyzed the switching behavior of Si MOSFETs under different load conditions [14], [15]. However, when analyzing the rising or falling speed of the drain-to-source voltage, these papers assume a Miller plateau always occurred. On the contrary, [14] and [17] claimed the gate voltage could be below the threshold voltage without a Miller plateau during the rising time of the drain-to-source voltage, but they did not analyze why and under what condition there is no Miller plateau. To thoroughly investigate the influence of the load conditions on the switching speed and the difference between Si MOSFETs and GaN HEMTs, the switching behavior of $\rm M_1$ is analyzed later based on the schematic and the voltages and currents at that time.

Because the switching speed is mainly determined by the parasitic capacitance of the switches [13], to investigate the switching speed difference between Si MOSFETs and GaN HEMTs, the parasitic capacitance $C_{\rm gd}$ between gate and drain, $C_{\rm gs}$ between gate and source and $C_{\rm ds}$ between drain and source in Fig. 8 will be considered. On the contrary, the influence of the common source inductance on the rising/falling speed of the drain-to-source voltage is limited, as a result, it is ignored as indicated in [12], [13], and [16].

From Fig. 5(b), the rising of $V_{\rm ds1}$ happens at t_0, when $\rm M_1$ is turned OFF by the driving signal $V_{\rm Drive1}$. On the other hand, its falling edge at t_2 is caused by the turning OFF of $\rm M_5$ due to the ZVS operation of the DAB converter. Therefore, both the rising and falling speeds are determined by the turn-OFF characteristics of the devices. Here, the turn-OFF transient of $\rm M_1$, corresponding to the rising edge of $V_{\rm ds1}$, will be analyzed as an example. The analysis of the falling edge, which is related to the turn-OFF of $\rm M_5$, is similar, so it will not be repeated here.

At t_0, $V_{\rm Drive1}$ is set to 0, and $V_{\rm Drive5}$ is still zero due to the dead time. $V_{\rm ds1}$ begins to increase. The current and

Authorized licensed use limited to: University of Florida. Downloaded on December 30,2020 at 03:23:17 UTC from IEEE Xplore. Restrictions apply.

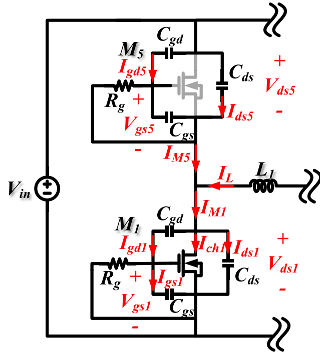

Fig. 9. Current and voltage distribution in the half bridge of M_1 and M_5 at t_0.

voltage distribution in the half bridge at this time is illustrated in Fig. 9.

From Fig. 9, at the gate of M_1, there are three currents—the current flowing through the driving resistor R_g, the charging/discharging currents I_{gd1}, and I_{gs1}. So

$$\frac{V_{\mathrm{gs1}}}{R_g} = C_{\mathrm{gd}} \frac{d(V_{\mathrm{ds1}} - V_{\mathrm{gs1}})}{dt} - C_{\mathrm{gs}} \frac{dV_{\mathrm{gs1}}}{dt}. \tag{4}$$

Meanwhile, at the drain of M_1, the current flowing through M_1 includes two parts: the channel current I_{ch1} and the charging/discharging currents I_{gd1} and I_{ds1}.

$$I_{M1} = C_{\mathrm{gd}} \frac{d(V_{\mathrm{ds1}} - V_{\mathrm{gs1}})}{dt} + C_{\mathrm{ds}} \frac{dV_{\mathrm{ds1}}}{dt} + I_{\mathrm{ch1}} \tag{5}$$

$$I_{ch1} = \frac{1}{2} K (V_{gs1} - V_{TH})^2. \tag{6}$$

Because the transconductance g_{fs} depends on V_{gs}, the calculation of the rising/falling speed will be inaccurate when g_{fs} is treated as a constant. Using the constant K to calculate the channel current in (6) solves this issue.

The input capacitance C_{iss} and the output capacitance C_{oss} are

$$C_{\mathrm{iss}} = C_{\mathrm{gs}} + C_{\mathrm{gd}} \tag{7}$$

$$C_{\mathrm{oss}} = C_{\mathrm{gd}} + C_{\mathrm{ds}}. \tag{8}$$

Therefore, (4)∼(6) can be reduced to

$$\frac{V_{\mathrm{gs1}}}{R_g} = C_{\mathrm{gd}} \frac{dV_{\mathrm{ds1}}}{dt} - C_{\mathrm{iss}} \frac{dV_{\mathrm{gs1}}}{dt} \tag{9}$$

$$I_{M1} = C_{\mathrm{oss}} \frac{dV_{\mathrm{ds1}}}{dt} - C_{\mathrm{gd}} \frac{dV_{\mathrm{gs1}}}{dt} + \frac{1}{2} K (V_{\mathrm{gs1}} - V_{\mathrm{TH}})^2. \tag{10}$$

Similarly, for M_5

$$\frac{V_{\mathrm{gs5}}}{R_g} = C_{\mathrm{gd}} \frac{dV_{\mathrm{ds5}}}{dt} - C_{\mathrm{iss}} \frac{dV_{\mathrm{gs5}}}{dt} \tag{11}$$

$$I_{M5} = C_{\mathrm{oss}} \frac{dV_{\mathrm{ds5}}}{dt} - C_{\mathrm{gd}} \frac{dV_{\mathrm{gs5}}}{dt}. \tag{12}$$

Because C_{oss} is always larger than C_{gd}, and dV_{ds5}/dt is much larger than dV_{gs5}/dt, we can simplify (12) as

$$I_{M5} = C_{\mathrm{oss}} \frac{dV_{\mathrm{ds5}}}{dt}. \tag{13}$$

Additionally

$$I_L = I_{M1} - I_{M5} \tag{14}$$

$$V_{\mathrm{in}} = V_{\mathrm{ds1}} + V_{\mathrm{ds5}}. \tag{15}$$

From (9), (10), and(13)–(15), the equation set to derive the rising speed of V_{ds1} is

$$\begin{cases} \frac{V_{\mathrm{gs1}}}{R_g} = C_{\mathrm{gd}} \frac{dV_{\mathrm{ds1}}}{dt} - C_{\mathrm{iss}} \frac{dV_{\mathrm{gs1}}}{dt} \\ I_L = 2C_{\mathrm{oss}} \frac{dV_{\mathrm{ds1}}}{dt} - C_{\mathrm{gd}} \frac{dV_{\mathrm{gs1}}}{dt} + \frac{1}{2} K (V_{\mathrm{gs1}} - V_{\mathrm{TH}})^2. \end{cases} \tag{16}$$

While solving the aforementioned equation, it is found that there is a critical current I_{L_crit} in (17) for I_L. I_{L_crit} is the minimum current needed to provide the channel current I_{ch1}, the charging and discharging current I_{gd1}, I_{gs1}, and I_{M5}. Depending on whether I_L is larger or smaller than I_{L_crit}, the rising speed of V_{ds1} is represented by different equations. Both cases are analyzed as follows:

$$I_{L-\mathrm{crit}} = \frac{2KR_g C_{\mathrm{gd}} V_{\mathrm{TH}} C_{\mathrm{oss}} - 2C_{\mathrm{oss}}^2}{K (R_g C_{\mathrm{gd}})^2}. \tag{17}$$

Case I. $I_L \geq I_{L-\mathrm{crit}}$: In this case, I_L is large enough to provide both the channel current I_{ch1} and all the charging/discharging currents. So M_1 is still ON when V_{ds1} rises. At this time, V_{gs1} and dV_{ds1}/dt are

$$V_{\mathrm{gs1}} = V_{\mathrm{TH}} + \frac{\sqrt{2KI_L (R_g C_{\mathrm{gd}})^2 - 4KR_g C_{\mathrm{gd}} V_{\mathrm{TH}} C_{\mathrm{oss}} + 4C_{\mathrm{oss}}^2} - 2C_{\mathrm{oss}}}{KR_g C_{\mathrm{gd}}} \tag{18}$$

$$\frac{dV_{\mathrm{ds1}}}{dt} = \frac{V_{\mathrm{TH}}}{R_g C_{\mathrm{gd}}} + \frac{\sqrt{2KI_L (R_g C_{\mathrm{gd}})^2 - 4KR_g C_{\mathrm{gd}} V_{\mathrm{TH}} C_{\mathrm{oss}} + 4C_{\mathrm{oss}}^2} - 2C_{\mathrm{oss}}}{K (R_g C_{\mathrm{gd}})^2}. \tag{19}$$

From (18) and (19), if C_{oss} and C_{gd} are constant, V_{gs1} does not change while the rising speed of V_{ds1} is also constant. However, since C_{oss} and C_{gd} are a function of V_{ds1}, V_{gs1} and rising speed would not be constant. R_g and C_{gd}, C_{oss} affect the rising speed.

Meanwhile, the currents flowing through the switches are

$$I_{M1} = I_{\mathrm{ch1}} + C_{\mathrm{oss}} \frac{dV_{\mathrm{ds1}}}{dt} \tag{20}$$

$$I_{M5} = -C_{\mathrm{oss}} \frac{dV_{\mathrm{ds1}}}{dt}. \tag{21}$$

If I_L is much larger than I_{L_crit}, the channel current of M_1 is much larger than the charging/discharging current. Then

$$I_{M1} \approx I_L \tag{22}$$

$$I_{M5} \approx 0. \tag{23}$$

And (18) and (19) can be further simplified as

$$V_{\mathrm{gs1}} = V_{\mathrm{TH}}$$

Authorized licensed use limited to: University of Florida. Downloaded on December 30,2020 at 03:23:17 UTC from IEEE Xplore. Restrictions apply.

$$+\frac{\sqrt{2KI_L(R_gC_{\rm gd})^2-4KR_gC_{\rm gd}V_{\rm TH}C_{\rm oss}+4C_{\rm oss}^2}-2C_{\rm oss}}{KR_gC_{\rm gd}}$$

$$=V_{\rm TH}+\frac{\sqrt{\begin{array}{l}(R_gC_{\rm gd}\sqrt{2KI_L}+2C_{\rm oss})^2\\ -4KR_gC_{\rm gd}C_{\rm oss}\left(V_{TH}+\sqrt{\frac{2I_L}{K}}\right)\end{array}}-2C_{\rm oss}}{KR_gC_{\rm gd}}$$

$$\approx V_{\rm TH}+\frac{R_gC_{\rm gd}\sqrt{2KI_L}+2C_{\rm oss}-2C_{\rm oss}}{KR_gC_{\rm gd}}=V_{\rm TH}+\sqrt{\frac{2I_L}{K}} \quad (24)$$

$$\frac{dV_{\rm ds1}}{dt}=\frac{V_{\rm TH}}{R_gC_{\rm gd}}$$

$$+\frac{\sqrt{2KI_L(R_gC_{\rm gd})^2-4KR_gC_{\rm gd}V_{\rm TH}C_{\rm oss}+4C_{\rm oss}^2}-2C_{\rm oss}}{K(R_gC_{\rm gd})^2}$$

$$\approx\frac{V_{TH}}{R_gC_{\rm gd}}+\frac{1}{R_gC_{\rm gd}}\sqrt{\frac{2I_L}{K}}. \quad (25)$$

Equations (24) and (25) agree with the equations in most textbooks and papers in the derivation of switching speed [13], [22]. Under this circumstance, the channel current $I_{\rm ch1}$ dominates I_L, so the rising speed is determined by R_g and $C_{\rm gd}$ in the driving loop as in (25). The results in (18) and (19) are close to those of (24) and (25).

Equations (24) and (25) could be inaccurate when $I_L \gg I_{L-{\rm crit}}$ is not met. Equations (18) and (19) should thus be used under that condition.

Case II. $I_L < I_{L-{\rm crit}}$*:* In this case, I_L is not enough to provide both the channel current $I_{\rm ch1}$ and all the charging/discharging currents.

As a result, the rising speed of $V_{\rm ds1}$ is mainly determined by the charging and discharging current

$$\frac{dV_{\rm ds1}}{dt}=\frac{I_L}{2C_{\rm oss}}. \quad (26)$$

So, the currents flowing through M_1 and M_5 are both determined by the charging and discharging currents

$$I_{M1}=C_{\rm oss}\frac{dV_{\rm ds1}}{dt} \quad (27)$$

$$I_{M5}=-C_{\rm oss}\frac{dV_{\rm ds1}}{dt}. \quad (28)$$

In conclusion, under different load conditions, depending on whether I_L is large enough to provide both the channel current and the charging/discharging currents, different equations ought to be applied to calculate the switching speed of the semiconductor devices.

As stated previously, the $V'_{\rm ds1}$s falling edge can be analyzed based on M_5's turning OFF, which is similar to M_1's analysis, so the conclusion is the same.

2) Comparison of Experimental Results of Si MOSFETs and GaN HEMTs: Based on the parameters of Si MOSFETs and GaN HEMTs in Table I, the critical current $I_{L_{\rm crit}}$ can be calculated

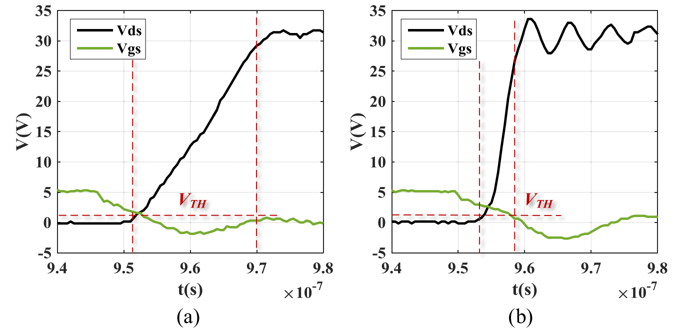

Fig. 10. $V_{\rm gs}$ and $V_{\rm ds}$ of M_1 under different load conditions: (a) output power is 49 W, $I_L = 1.8$ A, and (b) output power is 132 W, $I_L = 8.4$ A.

from (17) as

$$\text{Si MOSFETS}: I_{L_{\rm crit}}=4.2\text{ A} \quad (29)$$

$$\text{GaN HEMTs}: I_{L_{\rm crit}}=55.6\text{ A}. \quad (30)$$

From (30), due to the small $C_{\rm gd}$ of the GaN HEMT, its $I_{L_{\rm crit}}$ is even larger than the maximum drain current. Thus, the GaN HEMT only has case II. Namely, in the whole power range of the converter with GaN HEMTs, the GaN HEMT is always OFF during the rising and falling edges of $V_{\rm ds}$, and its speed is determined by I_L and $C_{\rm oss}$ in (26).

Different from the GaN HEMT, $I_{L_{\rm crit}}$ of the Si MOSFET falls within its maximum current range. Hence, it can have either case under different load conditions. The voltages on M_1 at the turn-OFF transient are measured in Fig. 10 to prove the influence of load conditions.

In Fig. 10(a), when $I_L < I_{L_{\rm crit}}$, at the rising edge of $V_{\rm ds}$, the gate-to-source voltage $V_{\rm gs}$ is already below $V_{\rm TH}$. While in Fig. 10(b), $V_{\rm gs}$ is always above $V_{\rm TH}$ when $V_{\rm ds}$ rises.

Fig. 11 shows the rising and falling edge of the Si MOSFET and the GaN HEMT under different load conditions. The rising and falling time is calculated and compared with the measured results in Table II.

From Table II, the calculated rising and falling time based on the proposed equations are almost equal to the measured results under different load conditions, therefore, they verified the equations. On the other hand, the calculated rising and falling time based on the conventional equation (25) is inaccurate for all cases when $I_L < I_{L-{\rm crit}}$. For the GaN HEMT in Table II, (25) always gives wrong results.

Based on the waveforms in Fig. 11 and the rising and falling time in Table II, for the same device, the rising and falling speeds are always faster under heavy load than that under light load because I_L is bigger under heavy load than under light load. Bigger I_L can provide more charging and discharging current to shorten the rising and falling time.

On the other hand, in Fig. 11, under light load, the rising and falling time of the Si MOSFET is close to that of the GaN HEMT as predicted in (26), causing by their similar output capacitance $C_{\rm oss}$. Under heavy load, the switching speeds of GaN HEMTs are determined by (26), on the other hand, the switching speeds of Si MOSFETs can be determined by either (19) or (26) depending

Authorized licensed use limited to: University of Florida. Downloaded on December 30,2020 at 03:23:17 UTC from IEEE Xplore. Restrictions apply.

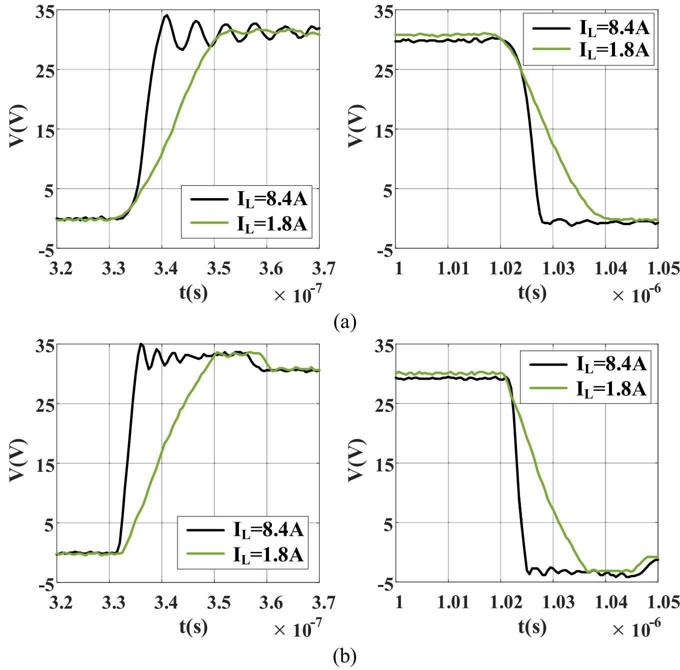

Fig. 11. Rising and falling edge of $V_{\rm ds}$ under different load conditions for (a) Si MOSFET and (b) GaN HEMT.

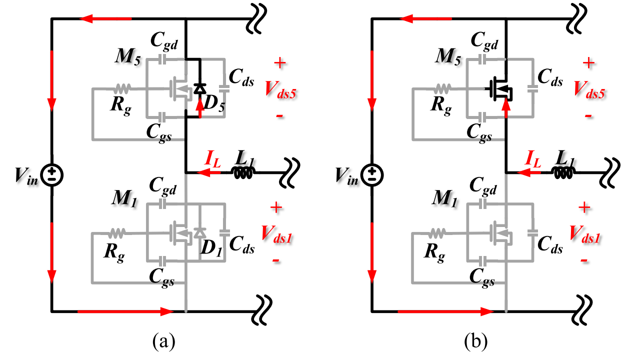

Fig. 12. Current distribution in the half bridge of M_1 and M_5 at the dead time t_0–t_1 after M_1 is turned OFF. (a) Si MOSFETs. (b) GaN HEMTs.

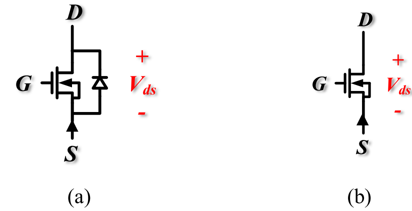

Fig. 13. Reverse voltage drop of a (a) Si MOSFET, and (b) GaN HEMT.

TABLE II
COMPARISON OF CALCULATED AND MEASURED RISING AND FALLING TIME OF THE Si MOSFET AND GaN HEMT UNDER DIFFERENT LOAD CONDITIONS

	Si MOSFET IRF7493		*GaN HEMT* LMG5200	
I_{L_crit} **(A)**	4.2		55.6	
I_L **(A)**	1.8	8.4	1.8	8.4
Case	Case II	Case I	Case II	Case II
Calculated dV_{ds}/dt (V/ns)	2.2	6.9	2.3	10.5
Calculated t_r and t_f based on proposed equations (10%~90%) (ns)	10.9	3.5	10.7	2.3
Calculated t_r and t_f based on conventional equation (25) (10%~90%) (ns)	2.89	3.6	0.27	0.24
Measured t_r and t_f (10%~90%) (ns)	11.9	3.5	11.4	2.5
Corner Frequency $1/\pi t_r$ **(MHz)**	26.7	90.9	28	127

on the relationship of I_L and $I_{L-\rm crit}$. For the converter in Fig. 1, because $I_L > I_{L-\rm crit}$, (19) is used to calculate the speed. Based on the parameters in Table I and (19) and (26), GaN HEMT is faster than Si MOSFETs. This agrees with Fig. 11.

Table II also shows the corner frequency determined by the rising time t_r and falling time t_f of the $V_{\rm ds}$ in the spectrum of the $V_{\rm ds}$ [23]. The spectrum of $V_{\rm ds}$ changes slope from –20 to –40 dB/dec at the corner frequency, so the higher the corner frequency, the higher the EMI spectrum after the corner frequency. In Table II, the GaN HEMT has higher corner frequency than the Si MOSFET, its EMI noise is, therefore, higher at high frequencies. Higher rising and falling slopes, therefore, lead to higher radiated EMI.

B. ZVS Waveform

1) Theoretical Analysis: During the dead time t_0–t_1 and t_2–t_3 of the half bridge, both driving signals of the top and bottom switches are zero, but one of the switches reversely conducts load current I_L. Therefore, there are two small pulses after the rising and falling edges and their magnitudes are equal to the reverse conduction voltage drop of the switch. The current distribution in the half bridge at the dead time t_0–t_1 after M_1 is turned OFF is shown in Fig. 12.

Due to the different semiconductor structures of the Si MOSFET and GaN HEMT, the reverse conduction voltage drops are determined by different factors. For the Si MOSFET in Fig. 13(a), the reverse conduction voltage drop $V_{{\rm ds}_Si}$ is the forward voltage drop of the body diode V_f

$$V_{\rm ds_Si} = -V_f. \tag{31}$$

Nevertheless, when it comes to the GaN HEMT, which has no body diode, in Fig. 13(b), the reverse current can still flow from source to drain [24]. Hence, the gate-to-drain voltage of the GaN HEMT is at least its threshold voltage

$$V_{\rm gd} \geq V_{\rm TH}. \tag{32}$$

Because during the dead time, the driving signal is zero

$$V_{\rm gs} = 0 \tag{33}$$

$$V_{\rm ds_GaN} = V_{\rm gs} - V_{\rm gd} = -V_{\rm gd} \leq -V_{\rm TH}. \tag{34}$$

2) Comparison of Experimental Results of Si MOSFETs and GaN HEMTs: The voltage waveforms during the dead time t_0–t_1

Authorized licensed use limited to: University of Florida. Downloaded on December 30,2020 at 03:23:17 UTC from IEEE Xplore. Restrictions apply.

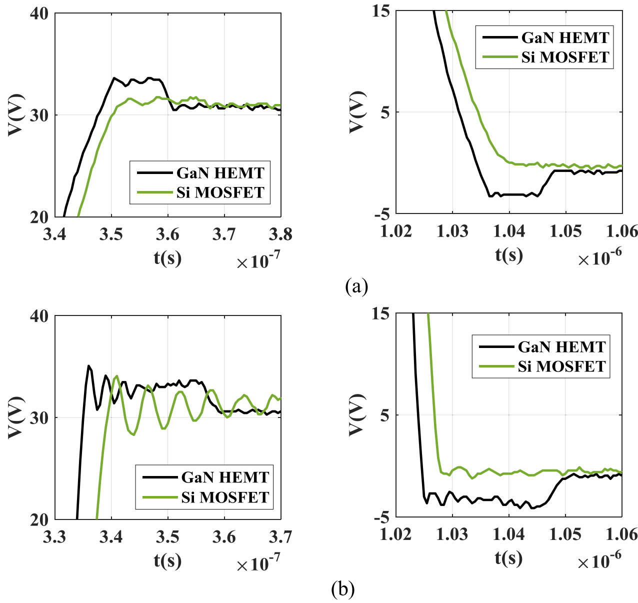

Fig. 14. Comparison of the voltage waveforms at the dead time t_0–t_1 and t_2–t_3 of Si MOSFETs and GaN HEMTs when (a) output power is 49 W, $I_L = 1.8$ A and (b) output power is 132 W, $I_L = 8.4$ A.

and t_2–t_3 are measured in Fig. 14. The magnitude of the ZVS pulses of the GaN HEMTs is about 2 V, while for the Si MOSFET, based on datasheet, it is only 0.6 V. Therefore, the ZVS voltage pulse of the Si MOSFET has much smaller effects on the spectrum of the total source voltage spectrum than the GaN HEMT, as shown in Fig. 7(a) and (c). On the contrary, the ZVS voltage pulse of the GaN HEMT may affect the spectrum of the total source voltage spectrum. Under light load, because the rising and falling slopes are slower than those under heavy load, within the radiated EMI frequency range, the spectrum is lower than that under heavy load, so the effects of ZVS voltage pulse on the total source voltage spectrum may become apparent as in Fig. 7(b).

C. Ringing

1) Theoretical Analysis: Due to the resonance of the parasitic parameters, the source voltages $V_{ds1} \sim V_{ds4}$ have ringing, which may cause severe EMI issues. The schematic of the half bridge consisting of M_1 and M_5 with the parasitic capacitance and inductance is illustrated in Fig. 15. L_{loop} is the parasitic loop inductance between the half bridge and C_{in}, while L_d and L_s are the combined parasitic inductance of the switch inductance and the trace inductance at the drain and the source connections, respectively.

Because of the low impedance of the input capacitor C_{in} at the ringing frequencies, the dc input voltage source V_{in} and the parasitic parameters between V_{in} and the input capacitor C_{in} have no influence on the ringing of V_{ds1}. Moreover, the inductance of L_1 is large enough so that the current flowing through it is constant at the turn-OFF transient. Hence, it does not affect the ringing, either.

The ringing of V_{ds1} occurs at the instant t_r at the end of rising edge when M_5 began to reversely turn ON and M_1 is still OFF. If

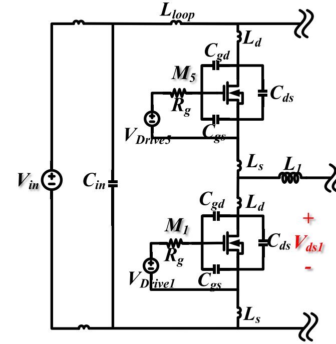

Fig. 15. Half bridge of M_1 and M_5 with parasitic capacitance and inductance.

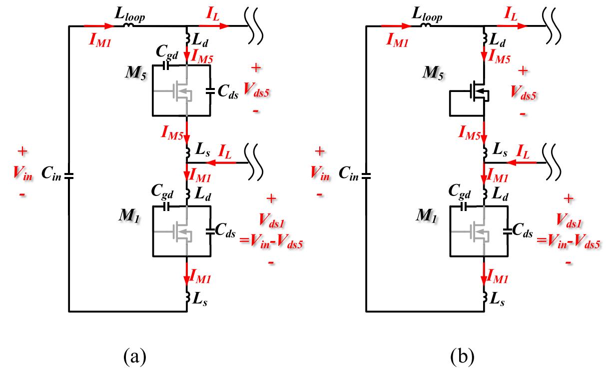

Fig. 16. Resonant circuit loop of V_{ds1} with its current and voltage distribution at (a) t_r^- and (b) t_r^+.

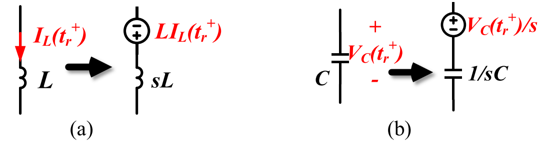

Fig. 17. Initial conditions are modeled as equivalent voltage sources for (a) inductor and (b) capacitor.

t_r^- is the time instant right before M_5 is ON and t_r^+ is the time instant right after M_5 is ON and the ringing begins, based on Fig. 15, the resonant circuit loop of V_{ds1} with its current and voltage distribution at t_r^- and t_r^+ is shown in Fig. 16. In Fig. 16, during the switching transient of the DAB converter, the top switch of the other half bridge is ON, so the load current I_L flows through the top switch of the other half bridge and back to the half bridge under investigation via the load, as shown in Fig. 16. Because of this, the current flowing through L_{loop} is the sum of I_{M5} and the load current I_L, which is equal to I_{M1}.

Referring to the properties of the Laplace transform, the initial conditions of the parasitic capacitance and inductance can be modeled as equivalent voltage sources [25] as Fig. 17. Therefore, the resonant circuit loop with the equivalent sources representing initial conditions is derived in Fig. 18(a).

Fig. 18(a) can be reduced to Fig. 18(b). In Fig. 18(b), E is the magnitude of the voltage source, which is determined by the

Authorized licensed use limited to: University of Florida. Downloaded on December 30,2020 at 03:23:17 UTC from IEEE Xplore. Restrictions apply.

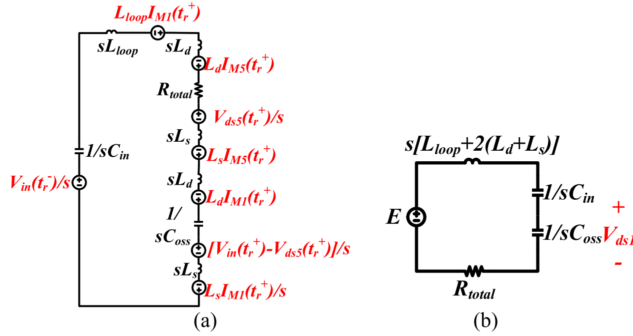

Fig. 18. Frequency-domain resonant circuit loop of V_{ds1} with equivalent voltage sources. (a) Original. (b) Reduced.

initial conditions

$$E = (L_{\text{loop}} + L_d + L_s)I_{M1}(t_r^+) + (L_d + L_s)I_{M5}(t_r^+). \tag{35}$$

And because the current flowing through the inductor cannot change instantaneously

$$I_{M1}(t_r^+) = I_{M1}(t_r^-) \tag{36}$$

$$I_{M5}(t_r^+) = I_{M5}(t_r^-) \tag{37}$$

$$E = (L_{\text{loop}} + L_d + L_s)I_{M1}(t_r^-) + (L_d + L_s)I_{M5}(t_r^-). \tag{38}$$

Then, the function for the ringing of V_{ds1} can be derived as

$$V_{\text{ds1_ringing}}(s) = \frac{E}{[L_{\text{loop}} + 2(L_d + L_s)]C_{\text{oss}}} \times \frac{1}{s^2 + s\frac{R_{\text{total}}}{[L_{\text{loop}}+2(L_d+L_s)]} + \frac{1}{[L_{\text{loop}}+2(L_d+L_s)]}\left(\frac{1}{C_{\text{in}}} + \frac{1}{C_{\text{oss}}}\right)}. \tag{39}$$

Because the capacitance of C_{in} is much larger than that of the output capacitance of the switches C_{oss}, (39) can be simplified as

$$V_{\text{ds1_ringing}}(s) = \frac{E}{[L_{\text{loop}} + 2(L_d + L_s)]C_{\text{oss}}} \times \frac{1}{s^2 + s\frac{R_{\text{total}}}{[L_{\text{loop}}+2(L_d+L_s)]} + \frac{1}{[L_{\text{loop}}+2(L_d+L_s)]C_{\text{oss}}}}. \tag{40}$$

Therefore, the time-domain waveform of the ringing is

$$V_{\text{ds1_ringing}}(t) = Ae^{-\alpha(t-t_r)} \sin[\omega_n(t - t_r)]\varepsilon(t - t_r) \tag{41}$$

$$A = \frac{\omega_0^2 E}{\omega_n} \tag{42}$$

$$\omega_0 = \frac{1}{\sqrt{[L_{\text{loop}} + 2(L_d + L_s)]C_{\text{oss}}}} \tag{43}$$

$$\alpha = \frac{R_{\text{total}}}{2[L_{\text{loop}} + 2(L_d + L_s)]} \tag{44}$$

$$\omega_n = \sqrt{\omega_0^2 - \alpha^2} \tag{45}$$

where A is the maximum magnitude of the ringing and is proportional to E, ω_0 is the natural resonant frequency, ω_n is the damped resonant frequency, and α is the damping coefficient.

From (35) and (41), besides the parasitic parameters, the initial currents flowing through the inductance also affect the magnitude of ringing. Because the parasitic inductance's initial current is different at different load conditions as analyzed for the two cases in Section III-A 1), the magnitudes of ringing are different under different load conditions.

1) *Case I.* $I_L \geq I_{L-\text{crit}}$: According to (20), (21), and (35), the equivalent voltage source E in Fig. 18(b) is

$$\begin{aligned} E &= (L_{\text{loop}} + L_d + L_s)I_{M1}(t_r^-) + (L_d + L_s)I_{M5}(t_r^-) \\ &= (L_{\text{loop}} + L_d + L_s)\left(I_{\text{ch1}} + C_{\text{oss}}\frac{dV_{\text{ds1}}}{dt}\right) \\ &\quad - (L_d + L_s)C_{\text{oss}}\frac{dV_{\text{ds1}}}{dt} \\ &= (L_{\text{loop}} + L_d + L_s)I_{ch1} + L_{\text{loop}}C_{\text{oss}}\frac{dV_{\text{ds1}}}{dt}. \end{aligned} \tag{46}$$

It is shown in (46) that, higher load currents result in higher magnitudes of ringing.

2) *Case II.* $I_L < I_{L-\text{crit}}$: From (26)–(28) and (35), the equivalent voltage source in this case is

$$\begin{aligned} E &= (L_{\text{loop}} + L_d + L_s)I_{M1}(t_r^-) + (L_d + L_s)I_{M5}(t_r^-) \\ &= (L_{\text{loop}}+L_d+L_s)C_{\text{oss}}\frac{dV_{\text{ds1}}}{dt} - (L_d+L_s)C_{\text{oss}}\frac{dV_{\text{ds1}}}{dt} \\ &= L_{\text{loop}}C_{\text{oss}}\frac{dV_{\text{ds1}}}{dt} = \frac{1}{2}L_{\text{loop}}I_L. \end{aligned} \tag{47}$$

For this case, the magnitude of ringing is also dependent on I_L. Higher load current will result in bigger ringing magnitude. Comparing (46) and (47), for the same device under different load conditions, due to higher dV_{ds1}/dt and the influence of the channel current I_{ch1}, the magnitude of ringing in the case I is always larger than that in the case II.

2) Comparison of Experimental Results of the Si MOSFET and the GaN HEMT: The waveforms and spectra of the ringing composition extracted from the measurements in Fig. 7 are compared in Fig. 19. As analyzed previously, depending on the load conditions, either case may occur on the converter with Si MOSFETs. When the load current is 8.4 A (the turn-OFF current at 132-W output power), it is case I, and while it is case II when the load current is 1.8 A (the turn-OFF current at 49-W output power). Therefore, in Fig. 19 (a), the magnitude of ringing with heavy load is larger than that with the light load as predicted in (46) and (47).

For the GaN HEMTs, although it only has case II, the dV_{ds1}/dt with heavy load is always higher than that with light load, leading to severer ringing.

On the other hand, comparing the ringing of Si MOSFETs and GaN HEMTs when I_L is 8.4 A, although they have similar C_{oss}, the equivalent voltage source E of the Si MOSFET is larger than that of the GaN HEMT based on (46) and (47). Moreover, while I_L is 1.8 A, the QFM package of the GaN HEMTs leads

Authorized licensed use limited to: University of Florida. Downloaded on December 30,2020 at 03:23:17 UTC from IEEE Xplore. Restrictions apply.

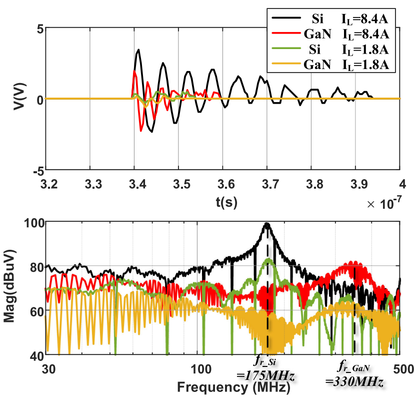

Fig. 19. Comparison of the ringing of Si MOSFETs and GaN HEMTs under different load conditions. (a) Time-domain waveforms. (b) Spectra.

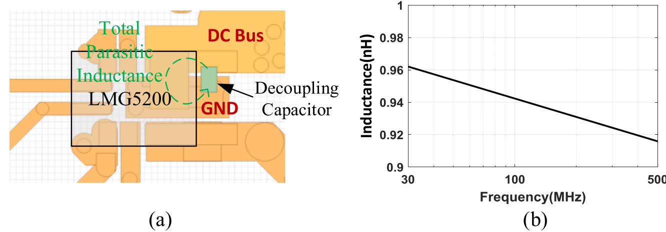

Fig. 20. Simulation of the loop inductance of the GaN HEMT half bridge. (a) Simulation model. (b) Simulated loop inductance.

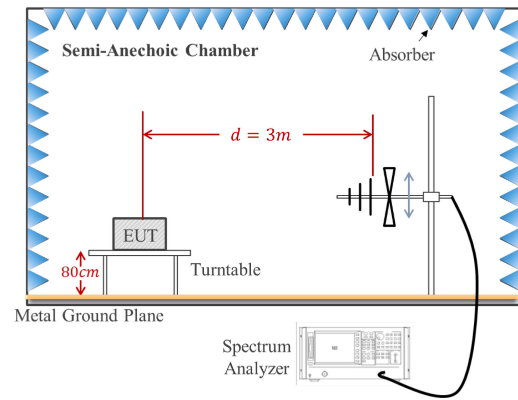

Fig. 21. Measurement setup of radiated EMI.

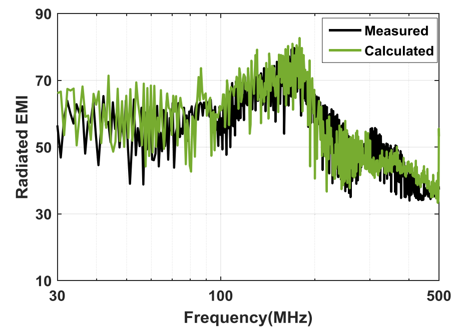

Fig. 22. Comparison of the calculated and measured radiated EMI generated by the converter with Si MOSFETs under heavy load.

to smaller parasitic inductance, therefore, resulting in smaller ringing and higher resonant frequency.

In Fig. 19, at the frequencies of the ringing, the spectra have spikes at 175 and 330 MHz. Based on Fig. 18, Table I, (43), and Fig. 19, the total inductance $L_{\text{loop}} + 2(L_d + L_s)$ of the resonant loops in Fig. 18 are calculated as 0.9 nH for the converter with GaN HEMTs and 2.9 nH for the converter with Si MOSFETs. Because the half bridge of the GaN HEMTs is integrated in one IC chip with QFM package and the decoupling capacitor is added very next to the chip, the loop inductance is much smaller than that of the discrete Si MOSFETs. The loop inductance of the GaN HEMT is also extracted using finite-element-analysis simulation in Fig. 20. It is around 0.94 nH very close to the calculated.

IV. Experimental Result

A. Comparison of Radiated EMI Generated by Converters With Si MOSFETs and GaN HEMTs

The radiated EMI generated by the converters was measured in a 3-m semianechoic chamber [7], [8]. The measurement setup is shown in Fig. 21. Based on the technique in [19] and the radiation model in Fig. 3, the radiated electric field of the board with Si MOSFETs under heavy load is calculated from (1) and compared with the measured in Fig. 22. They match very well. For the radiated EMI at light load or with GaN HEMTs, the calculations are similar, so they will not be repeated here.

According to Fig. 3, there are four noise sources $V_{\text{ds1}} \sim V_{\text{ds4}}$. The magnitude of the noise source spectra and the phase shift between the noise sources affect the radiated EMI. So, the final measured spectrum of the radiated EMI is determined by the four noise sources instead of one. As a result, the spectrum difference of the noise sources between Si MOSFETs and GaN HEMTs may not exactly match the spectrum difference of the measured radiated EMI in the whole frequency range. The measured radiated EMI spectra are compared with the spectra of the four noise sources at 49- and 132-W load in Fig. 23.

Although the waveforms of the four sources are similar in Fig. 4, their spectra could be different especially between the sources on the primary side and those on the secondary side due to the load current difference of the primary side and secondary side. Under light load, the primary-load current is 1.8 A, while that of the secondary side is 2.8 A. Therefore, the switching speeds of the semiconductor switches on the secondary side are faster than those on the primary side, causing higher noise spectra at low frequencies in Fig. 23(a).

On the contrary, when the converter is under heavy load, the primary-side load current is 8.4 A and the secondary-side load current is 9.2 A. Therefore, the difference between switching speeds is very small, leading to similar source voltage spectra in Fig. 23(b).

From Fig. 23, the difference of the radiated EMI is corresponding to the difference between source voltage spectra. First, under the same load condition, the switching speed of the GaN HEMT is faster than that of the Si MOSFET, leading to higher magnitude of the trapezoidal wave spectrum within the radiated EMI frequency range as analyzed in Section III-A 2).

Authorized licensed use limited to: University of Florida. Downloaded on December 30,2020 at 03:23:17 UTC from IEEE Xplore. Restrictions apply.

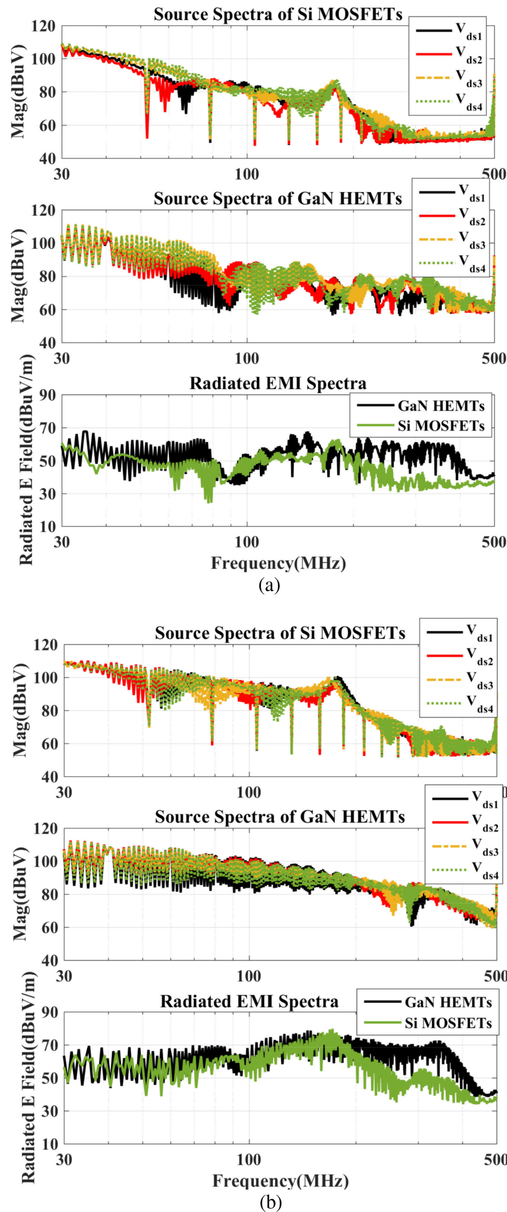

Fig. 23. Comparison of source voltage spectrum and radiated EMI between the converter with Si MOSFETs and GaN HEMTs under different load conditions: (a) output power is 49 W and (b) output power is 132 W.

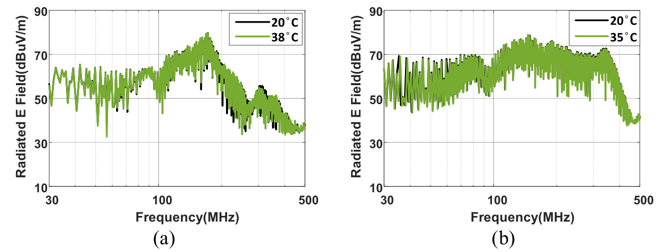

Fig. 24. Comparison of the radiated EMI at different semiconductor device case temperatures. (a) Si-MOSFET converter with 132-W output power. (b) GaN-HEMT converter with 132-W output power.

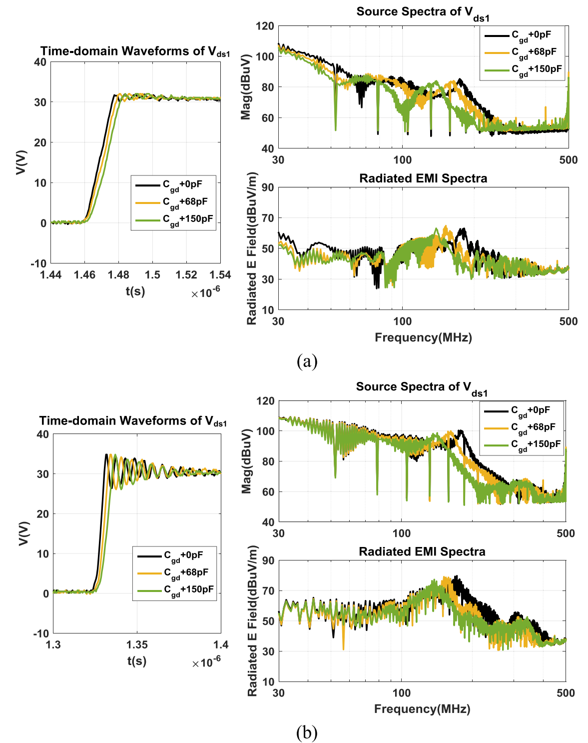

Fig. 25. Comparison of time-domain waveforms, source voltage spectra, and radiated EMI with different C_{gd} when (a) output power is 49 W and (b) output power is 132 W.

Meanwhile, the GaN HEMT also has larger reverse conduction voltage, so the spectrum due to ZVS waveform of the GaN HEMT is higher than that due to the Si MOSFET as well. Moreover, although the magnitude of ringing of the GaN HEMT is lower than that of the Si MOSFET, it can still generate a significant high frequency spectrum spike due to its higher resonant frequency. Consequently, the voltage source spectra of the converter with GaN HEMTs are higher than those with the Si MOSFETs in the corresponding frequency range.

By comparing Fig. 23(a) with (b), it is concluded that under different load conditions, the voltage source spectrum and the radiated EMI are both higher under heavy load than those under light load due to the faster switching speeds and higher initial currents of the ringing under heavy load.

In addition, the impedance of the parasitic parameters changes slightly at different temperatures according to the datasheets of the semiconductor devices. However, its effect on the radiated EMI is ignorable due to the very limited parasitic impedance variation. The radiated EMI at different temperatures is measured and compared in Fig. 24. The case temperature of the semiconductor switches is measured using a Fluke 62 max IR infrared thermometer.

B. Influence of Parasitic Parameters on Radiated EMI

Based on previous analysis, the difference between the radiation generated by converters with Si MOSFETs and GaN HEMTs at different load conditions is due to their different switching characteristics that are determined by their parasitic parameters. To further clarify the effect of parasitic parameters on the radiated EMI, the radiated EMI generated by the Si MOSFET converter with different parasitic parameters is compared.

Authorized licensed use limited to: University of Florida. Downloaded on December 30,2020 at 03:23:17 UTC from IEEE Xplore. Restrictions apply.

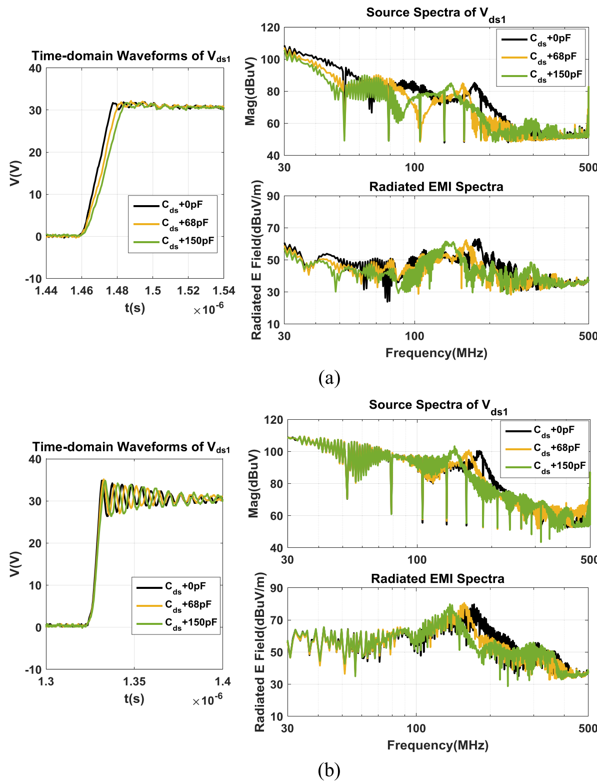

Fig. 26. Comparison of time-domain waveforms, source voltage spectra, and radiated EMI with different $C_{\rm ds}$ when (a) output power is 49 W and (b) output power is 132 W.

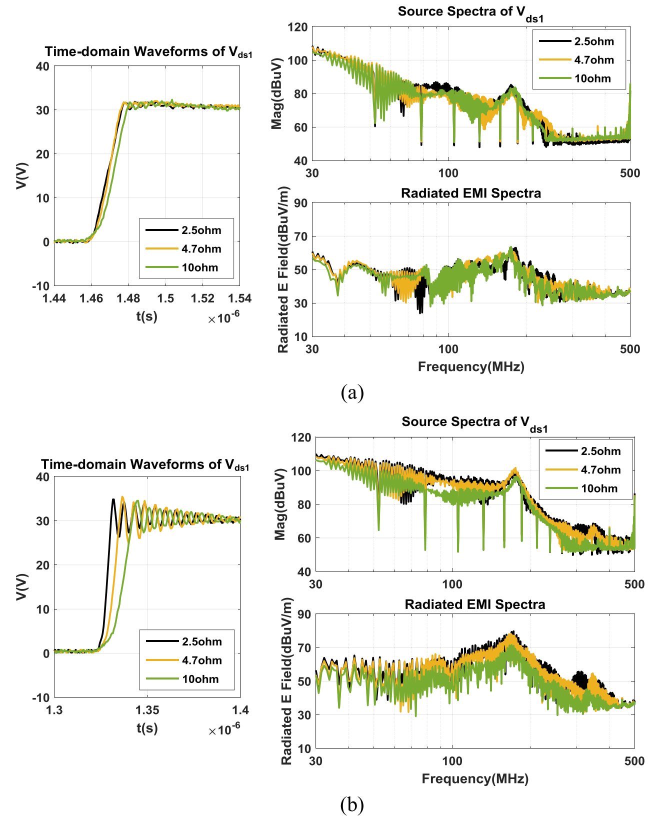

Fig. 27. Comparison of time-domain waveforms, source voltage spectra and radiated EMI with different R_g when (a) output power is 49 W and (b) output power is 132 W.

First, $C_{\rm gd}$ is equivalently changed by adding small capacitances between the gate and drain of the MOSFETs. The time-domain waveform of $V_{\rm ds1}$, the corresponding source voltage spectrum and the radiated EMI are compared in Fig. 25.

In Fig. 25(a), when the converter is under light load, increasing $C_{\rm gd}$ increases the output capacitance $C_{\rm oss}$ in (26), therefore, decreasing the switching speed of the MOSFETs. As a result, the magnitudes of the source voltage spectrum and the radiated EMI decrease at low frequencies where the trapezoidal waveform dominates. Meanwhile, it reduces the resonant frequency based on (43).

On the other hand, when the converter is under heavy load, increasing $C_{\rm gd}$ directly decreases the switching speed based on (25). This leads to increased rising and falling time that only reduces the spectrum after the corner frequency, as given by Table II, which is around 50 MHz when 150 pF is added and 66 MHz when 68 pF is added. Besides, increasing $C_{\rm gd}$ also reduces the resonant frequency.

Second, the drain-to-source capacitance $C_{\rm ds}$ is changed by adding small capacitances. The spectra of $V_{\rm ds1}$ and radiated EMI are compared in Fig. 26.

In Fig. 26(a), when the converter is under light load, increasing $C_{\rm ds}$ increases the output capacitance $C_{\rm oss}$, which has the same effect of increasing $C_{\rm gd}$. Therefore, the spectra in Fig. 26(a) are similar to those in Fig. 25(a).

On the contrary, when the converter is under heavy load, $C_{\rm ds}$ has limited effect on the switching speed of the MOSFETS according to (25). Hence, the spectra of the source voltage and the radiated EMI with different $C_{\rm ds}$ are the same at low frequencies in Fig. 26, while the resonant frequency decreases with the increased $C_{\rm ds}$.

Finally, the driving resistor R_g is changed from 2.5 to 4.7 Ω and 10 Ω. The results are shown in Fig. 27.

In Fig. 27(a), when the converter is under light load, based on (17), while R_g is changed from 2.5 to 4.7 Ω, it is the case II. Therefore, the rising speed of the source voltage is only related to $C_{\rm oss}$ in (26). Consequently, the time-domain waveform, source voltage spectrum and radiated EMI are almost the same as those when R_g is 2.5 Ω.

However, when R_g is 10 Ω, according to (17), it is case I. Therefore, the rising speed of $V_{\rm ds1}$ is reduced and the magnitudes of the corresponding source spectrum and radiated EMI are reduced within the whole frequency range.

On the contrary, when the converter is under heavy load, R_g will directly affect the switching speed based on (25). Hence, the difference of time-domain waveforms, source voltage spectra and radiated EMI with different R_g is obvious in Fig. 27(b).

V. Conclusion

It was concluded in this article that, at the identical operating conditions, GaN HEMTs had higher rising and falling slopes, higher ZVS voltage drops, and higher ringing frequencies, despite of lower ringing magnitudes, than Si MOSFETs. As a result, GaN HEMTs had higher radiated EMI than Si MOSFETs. For

Authorized licensed use limited to: University of Florida. Downloaded on December 30,2020 at 03:23:17 UTC from IEEE Xplore. Restrictions apply.

both GaN HEMTs and Si MOSFETs, heavy load always leads to higher radiated EMI than light load. Besides, at low frequencies, the radiated EMI was mainly affected by the raising/falling speed of the switches. Therefore, R_g and C_{gd} were key factors under heavy load, while C_{oss} dominates under light load. On the contrary, when the influence of the ringing becomes significant at high frequencies, the parasitic inductance and C_{oss} had dominant impact on the radiated EMI.

REFERENCES

[1] Z. Liu, "Characterization and failure mode analysis of cascode GaN HEMT," Master of Science thesis, Dept. Elect. Eng., Virginia Polytechnic Inst. and State Univ., Blacksburg, VA, USA, 2014.

[2] J. Millán, P. Godignon, X. Perpiñà, A. P.-Tomás, and J. Rebollo, "A survey of wide bandgap power semiconductor devices," *IEEE Trans. Power Electron.*, vol. 29, no. 5, pp. 2155–2163, May 2014.

[3] E. A. Jones, F. F. Wang, and D. Costinett, "Review of commercial GaN power devices and GaN-based converter design challenges," *IEEE J. Emerg. Sel. Topics Power Electron*, vol. 4, no. 3, pp. 707–719, Sep. 2016.

[4] X. Huang, Z. Liu, Q. Li, and F. C. Lee, "Evaluation and application of 600 V GaN HEMT in cascode structure," in *Proc. 28th Annu. Appl. Power Electron. Conf. Expo.*, 2013, pp. 1279–1286.

[5] E. A. Jones, "Review and characterization of gallium nitride power devices," Master of Science thesis, Dept. Elect. Eng., Univ. Tennessee, Knoxville, TN, USA, 2016.

[6] D. Han, S. Li, Y. Wu, W. Choi, and B. Sarlioglu, "Comparative analysis on conducted CM EMI emission of motor drives: WBG versus Si devices," *IEEE Trans. Ind. Electron.*, vol. 64, no. 10, pp. 8353–8363, Oct. 2017.

[7] *FCC 47 CFR Part 15 Subpart B*, Federal Communications Commission, Washington, DC, USA, 2015.

[8] *Information Technology Equipment—Radio Disturbance Characteristics—Limits and Methods of Measurement*, ICT Standard EN 55022, 2010.

[9] D. Han, C. T. Morris, W. Lee, and B. Sarlioglu, "A case study on common mode electromagnetic interference characteristics of GaN HEMT and Si MOSFET power converters for EV/HEVs," *IEEE Trans. Transp. Electrific.*, vol. 3, no. 1, pp. 168–179, Mar. 2017.

[10] Y. Xiong, S. Sun, H. Jia, P. Shea, and Z. J. Shen, "New physical insights on power MOSFET switching losses," *IEEE Trans. Power Electron.*, vol. 24, no. 2, pp. 525–531, Feb. 2009.

[11] F. Krismer and J. W. Kolar, "Accurate power loss model derivation of a high-current dual active bridge converter for an automotive application," *IEEE Trans. Ind. Electron.*, vol. 57, no. 3, pp. 881–891, Mar. 2010.

[12] Z. Chen, D. Boroyevich, and R. Burgos, "Experimental parametric study of the parasitic inductance influence on MOSFET switching characteristics," in *Proc. Int. Power Electron. Conf.*, 2010, pp. 164–169.

[13] J. Wang, H. S. h. Chung, and R. T. h. Li, "Characterization and experimental assessment of the effects of parasitic elements on the MOSFET switching performance," *IEEE Trans. Power Electron.*, vol. 28, no. 1, pp. 573–590, Jan. 2013.

[14] Y. Ren, M. Xu, J. Zhou, and F. C. Lee, "Analytical loss model of power MOSFET," *IEEE Trans. Power Electron.*, vol. 21, no. 2, pp. 310–319, Mar. 2006.

[15] W. Eberle, Z. Zhang, Y. Liu, and P. C. Sen, "A practical switching loss model for buck voltage regulators," *IEEE Trans. Power Electron.*, vol. 24, no. 3, pp. 700–713, Mar. 2009.

[16] X. Huang, Q. Li, Z. Liu, and F. C. Lee, "Analytical loss model of high voltage GaN HEMT in cascode configuration," *IEEE Trans. Power Electron.*, vol. 29, no. 5, pp. 2208–2219, May 2014.

[17] E. A. Jones, Z. Zhang, and F. Wang, "Analysis of the dv/dt transient of enhancement-mode GaN FETs," in *Proc. IEEE Appl. Power Electron. Conf. Expo.*, 2017, pp. 2692–2699.

[18] Z. Zhang, B. Guo, and F. Wang, "Evaluation of switching loss contributed by parasitic ringing for fast switching wide band-gap devices," *IEEE Trans. Power Electron.*, vol. 34, no. 9, pp. 9082–9094, Sep.2019.

[19] Y. Zhang, S. Wang, and Y. Chu, "Investigation of radiated electromagnetic interference for an isolated high frequency DC-DC power converter with power cables," *IEEE Trans. Power Electron.*, vol. 34, no. 10, pp. 9632–9643, Oct. 2019.

[20] C. A. Balanis, *Antenna Theory: Analysis and Design*, 3rd ed. New York, NY, USA: Wiley, 2016.

[21] D. Costinett, D. Maksimovic, and R. Zane, "Design and control for high efficiency in high step-down dual active bridge converters operating at high switching frequency," *IEEE Trans. Power Electron.*, vol. 28, no. 8, pp. 3931–3940, Aug. 2013.

[22] B. J. Baliga, *Fundamentals of Power Semiconductor Devices*. Switzerland: Springer, 2010.

[23] Y. Zhang, S. Wang, and Y. Chu, "Comparison of radiated electromagnetic interference (EMI) generated by power converters with silicon MOSFETs and GaN HEMTs," in *Proc. IEEE Appl. Power Electron. Conf. Expo.*, 2019, pp. 1375–1382.

[24] E. A. Jones, F. Wang, and B. Ozpineci, "Application-based review of GaN HFETs," in *Proc. IEEE Workshop Wide Bandgap Power Devices Appl.*, 2014, pp. 24–29.

[25] A. S. W. Alan, V. Oppenheim and S. Hamid Nawab, *Signal and Systems*. Englewood Cliffs, NJ, USA: Prentice-Hall, 1982.

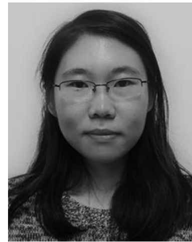

Yingjie Zhang (Student Member, IEEE) received the B.S.E.E. and M.S.E.E. degrees from the Huazhong University of Science and Technology, Wuhan, China, in 2013 and 2015, respectively. She is currently working toward the Ph.D. degree with the University of Florida, Gainesville, FL, USA.

Her research interests include electromagnetic interference in power converters and wide bandgap devices.

Shuo Wang (Fellow, IEEE) received the Ph.D. degree in electrical engineering from Virginia Tech, Blacksburg, VA, USA, in 2005.

He is currently a Full Professor with the Department of Electrical and Computer Engineering, University of Florida, Gainesville, FL, USA. He has authored and coauthored more than 190 IEEE journal and conference papers and holds around 30 pending/issued US/international patents.

Dr. Wang was the recipient of the Best Transaction Paper Award from the IEEE Power Electronics Society in 2006 and two William M. Portnoy Awards for the papers published in the IEEE Industry Applications Society in 2004 and 2012, respectively. He was also the recipient of the prestigious National Science Foundation CAREER Award, in 2012. He is an Associate Editor for the IEEE TRANSACTIONS ON INDUSTRY APPLICATIONS and a Technical Program Co-Chair for the IEEE 2014 International Electric Vehicle Conference.

Yongbin Chu received the B.S.E.E degree from the Hefei University of Technology, Hefei, China, in 2011, and the Ph.D. degree from the University of Texas at San Antonio, San Antonio, TX, USA, in 2015.

Since 2016, he has been with Texas Instruments Kilby Labs, Dallas, TX, USA. He has authored and coauthored more than 15 IEEE journal and conference papers. His research interests include electromagnetic interference/electromagnetic compatibility in power electronics systems, high-efficiency and high-power-density power conversion, and circuit topologies for power electronics.

Authorized licensed use limited to: University of Florida. Downloaded on December 30,2020 at 03:23:17 UTC from IEEE Xplore. Restrictions apply.